Published in final edited form as:

J Am Chem Soc. 2021 June 09; 143(22): 8237–8243. doi:10.1021/jacs.1c02323.

Vibrational Perturbation of the [FeFe] Hydrogenase H-Cluster Revealed by $^{13}C^{2}H$-ADT Labeling

Vladimir Pelmenschikov,
Institut für Chemie, Technische Universität Berlin, 10623 Berlin, Germany;

James A. Birrell,
Max Planck Institute for Chemical Energy Conversion, 45470 Mülheim an der Ruhr, Germany;

Leland B. Gee,
Department of Chemistry, Stanford University, Stanford, California 94305, United States;

Casseday P. Richers,
School of Chemical Sciences, University of Illinois, Urbana, Illinois 61801, United States;

Edward J. Reijerse,
Max Planck Institute for Chemical Energy Conversion, 45470 Mülheim an der Ruhr, Germany;

Hongxin Wang,
SETI Institute, Mountain View, California 94043, United States;

Simon Arragain,
IFP Energies nouvelles, 92852 Rueil-Malmaison, France; Department of Chemistry, University of California, Davis, California 95616, United States;

Nakul Mishra,
Department of Chemistry, University of California, Davis, California 95616, United States;

Yoshitaka Yoda,
Precision Spectroscopy Division, SPring-8/JASRI, Sayo, Hyogo 679-5198, Japan;

Hiroaki Matsuura,
Life Science Research Infrastructure Group, Advanced Photon Technology Division, RIKEN/SPring-8 Center, Sayo, Hyogo 679-5148, Japan;

Lei Li,

Corresponding Authors: **James A. Birrell** – Max Planck Institute for Chemical Energy Conversion, 45470 Mülheim an der Ruhr, Germany; james.birrell@cec.mpg.de**, Thomas B. Rauchfuss** – School of Chemical Sciences, University of Illinois, Urbana, Illinois 61801, United States; rauchfuz@illinois.edu**, Stephen P. Cramer** – SETI Institute, Mountain View, California 94043, United States; scramer@seti.org.

Supporting Information

The Supporting Information is available free of charge at https://pubs.acs.org/doi/10.1021/jacs.1c02323.
Experimental and computational procedures and additional data and figures including FTIR spectra, ^{57}Fe-PVDOS results, and relative displacements (PDF) Animated vibrational modes of the H_{hyd} DFT model as GIF files (ZIP)
Animated vibrational modes of the precursor DFT model as GIF files (ZIP)
Coordinates of the precursor, H_{hyd}, and H_{ox} DFT models as XYZ files (ZIP)

Complete contact information is available at: https://pubs.acs.org/10.1021/jacs.1c02323

The authors declare no competing financial interest.

Hyogo Science and Technology Association, Synchrotron Radiation Research Center, Tatsuno-shi, Hyogo 679-5165, Japan;

Kenji Tamasaku,
Research and Utilization Division, SPring-8/JASRI, Sayo, Hyogo 679-5198, Japan;

Thomas B. Rauchfuss,
School of Chemical Sciences, University of Illinois, Urbana, Illinois 61801, United States;

Wolfgang Lubitz,
Max Planck Institute for Chemical Energy Conversion, 45470 Mülheim an der Ruhr, Germany;

Stephen P. Cramer
SETI Institute, Mountain View, California 94043, United States;

Abstract

[FeFe] hydrogenases are highly active catalysts for the interconversion of molecular hydrogen with protons and electrons. Here, we use a combination of isotopic labeling, ^{57}Fe nuclear resonance vibrational spectroscopy (NRVS), and density functional theory (DFT) calculations to observe and characterize the vibrational modes involving motion of the 2-azapropane-1,3-dithiolate (ADT) ligand bridging the two iron sites in the $[2Fe]_H$ subcluster. A $-^{13}C^2H_2-$ ADT labeling in the synthetic diiron precursor of $[2Fe]_H$ produced isotope effects observed throughout the NRVS spectrum. The two precursor isotopologues were then used to reconstitute the H-cluster of [FeFe] hydrogenase from *Chlamydomonas reinhardtii* (*Cr*HydA1), and NRVS was measured on samples poised in the catalytically crucial H_{hyd} state containing a terminal hydride at the distal Fe site. The $^{13}C^2H$ isotope effects were observed also in the H_{hyd} spectrum. DFT simulations of the spectra allowed identification of the ^{57}Fe normal modes coupled to the ADT ligand motions. Particularly, a variety of normal modes involve shortening of the distance between the distal Fe–H hydride and ADT N–H bridgehead hydrogen, which may be relevant to the formation of a transition state on the way to H_2 formation.

Molecular hydrogen is viewed as an ideal carbon-free energy carrier that could be part of a transition to a sustainable economy without CO_2 emissions.[1,2] At the moment, the majority of industrial hydrogen is produced by high-temperature steam reforming of natural gas which leads to the release of at least one molecule of CO_2 for every 4 H_2 produced.[3] Ideally, electrochemical energy from solar, wind, or other carbon-free sources could be used to drive the water-splitting or "hydrogen evolution reaction" (HER) without CO_2 release.[1,4] Highly efficient catalysts with low overpotentials are essential for electrochemical conversions of hydrogen, and the high prices and scarcity of the current Pt or other noble metal HER catalysts have led to the search for systems that use earth-abundant materials.[5–7] One source of inspiration driving this search is Nature, which uses plentiful transition metals Fe or Fe with Ni in the active sites of hydrogenases.[8,9]

Hydrogenases are enzymes that catalyze the reversible interconversion of molecular hydrogen with protons and electrons: $H_2 \rightleftharpoons 2H^+ + 2e^-$. [FeFe] hydrogenases contain an active site "H-cluster" consisting of a $[4Fe–4S]_H$ cluster linked via a cysteine residue to a unique $[2Fe]_H$ subcluster (Figure 1a).[11] This subcluster carries a 2-azapropane-1,3-dithiolate

(ADT) ligand bridging a pair of CO and CN^- ligated Fe ions. The ADT bridgehead nitrogen has been implicated as part of a proton transfer relay extending through a neighboring cysteine.[12–16] In the *Chlamydomonas reinhardtii* [FeFe] hydrogenase (*Cr*HydA1), the conserved relay consists of C169, a water molecule, and oxygens from E141, S189, and E144 residues.

An iron hydride form of [FeFe] hydrogenase, H_{hyd}, is a key intermediate of the catalytic cycle, and it has been studied by multiple spectroscopic and molecular modeling techniques.[17–24] The H_{hyd} species contains a terminal Fe_d–H_h (hydride) at the $[2Fe]_H$ iron site distal to $[4Fe–4S]_H$ (Figure 1b), with a $[4Fe–4S]_H^+$ –$Fe_p(II)Fe_d(II)$ redox state for the H-cluster, along with the –NH_{ADT}– amine form of the ADT bridgehead.[18–21]

Nuclear resonance vibrational spectroscopy (NRVS) has become a popular technique for elucidating the element-selective normal modes of appropriate Mössbauer isotopes.[25–31] In previous work on the *Cr*HydA1 and *Dd*HydAB (from *Desulfovibrio desulfuricans*) enzymes,[20–22] we have shown that $^{57}Fe_d$–H_h bending modes can be observed using ^{57}Fe-NRVS for the H_{hyd} species and that these modes exhibit peak positions that are characteristic of the local environment. To better identify additional normal modes of H_{hyd}, we proceeded to label the $[2Fe]_H$ subcluster not only with ^{57}Fe but also with ^{13}C and D in the methylene groups of the ADT ligand. We accomplished this by preparing a $[2Fe]_H$ precursor, the ^{57}Fe-labeled salt $(Et_4N)_2$ [$^{57}Fe_2[(SCH_2)_2NH]$-$(CN)_2(CO)_4$] (**1**) as well as its variant also labeled with ^{13}C and D on the two methylene groups of the ADT ligand (**^{13}CD-1**).[32] We then used these samples to reconstitute an apo form of *Cr*HydA1 containing the $[4Fe–4S]_H$ cluster but lacking the $[2Fe]_H$ subsite.[33]

We first examine NRVS spectra for the precursor isotopologues **1** vs **^{13}CD-1** in Figure 2a. Close inspection reveals a number of subtle changes to band positions and intensities in the broad ~100–700 cm^{-1} range, most of them well reproduced by the DFT simulation shown in Figure 2b. We note that this is the first demonstration of NRVS isotope shifts from labeling in the second and third coordination spheres of ^{57}Fe, although such shifts have been seen before in resonance Raman spectra.[34,35] In the following, when referring to the bands observed (or vibrational frequencies calculated) for the two isotopologues, we use a nomenclature $x \rightarrow y$ (cm^{-1}) where x and y represent **1** and **^{13}CD-1**, respectively.

Since the bands from 400 to 660 cm^{-1} are dominated by Fe–CN and Fe–CO motions, we focus instead on differences in the region from 100 to 350 cm^{-1}, which contains delocalized bending and torsional modes as well as Fe–S stretching. In the **^{13}CD-1** spectra, several bands exhibit clear downshifts from the (^{12}CH–)**1** data, for example, at 150 → **139**, 168 → **164**, and 260 → **256** cm^{-1} (Figure 2a). This pattern is echoed in the **^{13}CD-1** DFT simulations, with downshifted bands at 161 → **143**, 173 → **168**, and 273 → **265** cm^{-1} (Figure 2b). The normal-mode analysis also reveals an isotope-dependent redistribution of the intensities underlying the DFT bands at 326 → **329**/**314** cm^{-1}, mapping onto the NRVS features at 322 → **326**/**302** cm^{-1}.

Having identified the most significant isotope shifts in the precursor spectra, we now illustrate the atomic motions deduced from the DFT calculations. As displayed in Figure 2

for **^{13}CD-1**, the normal mode calculated at **143** cm^{-1} is mostly out-of-phase rotation of the two ADT $–\mu S^{13}CD_2–$ groups around their S–C axes, combined with some motion of the μS pivot points due to Fe–S–Fe bending (see animated representations of the calculated vibrational modes as part of the Supporting Information and their characterization in Table S2). The large amount of methylene motion explains the significant isotope shift. In contrast, the **168** cm^{-1} mode involves rocking of the entire $–D_2{}^{13}C–NH–{}^{13}CD_2–$ assembly in one direction while the underlying Fe_2S_2 cluster (and associated ligands) rotates in the opposite direction. At higher frequencies, the **264** cm^{-1} mode involves out-of-phase displacements of the $–\mu S^{13}CD_2–$ fragments with substantial Fe–S stretching character, while the **314** cm^{-1} mode is an in-phase $–{}^{13}CD_2–$ methylene group motion, accompanied by wagging of the –NH– bridgehead in the opposite direction.

Our key observations from these precursor studies are (i) that the ^{13}CD substitution in the Fe-bridging ADT ligand induces measurable isotope shifts in the ^{57}Fe NRVS spectra, on the order of the 8 cm^{-1} instrumental resolution; (ii) that the DFT calculations are sufficiently accurate to reproduce these shifts, allowing confidence in the motions assigned to these modes; and (iii) that the calculations predict a variety of ADT flexing modes with significant motion of the –NH– bridgehead.

Precursors **1** and **^{13}CD-1** were used for maturation of the apo *Cr*HydA1 containing natural-abundance Fe in the $[4Fe–4S]_H$ cluster. This yielded holo *Cr*HydA1 labeled with ^{57}Fe in the $[2Fe]_H$ subcluster, and with either a natural-abundance ADT ligand (**1**-*Cr*HydA1) or $–{}^{13}CD_2–$ in the methylene portions of ADT (**^{13}CD-1**-*Cr*HydA1). These samples were poised in the H_{hyd} state by reduction with 100 mM sodium dithionite at pH 6. As shown by infrared (IR) spectra in Figure S1, both samples exhibited the standard H_{hyd} IR signature, with minimal contributions from other redox states.

NRVS data for **1**-*Cr*HydA1 and **^{13}CD-1**-*Cr*HydA1 are shown in Figure 3a, with the corresponding DFT simulations in Figure 3b. The calculated spectra were generated using a DFT model of H_{hyd} including the entire H-cluster and its immediate protein environment;[21,22,36] see DFT methods and model coordinates in the Supporting Information for further details. Again, we focus first on differences in the low-energy region, where we see the most obvious isotope effects. These include NRVS downshifts at 281 → **274** and 313 → **305** cm^{-1}, with the DFT simulations yielding corresponding modifications at 296 → **290** and 314 → **308** cm^{-1}. The 150–200 cm^{-1} isotope-dependent NRVS region (~174 → **166** cm^{-1}) of H_{hyd} essentially repeats in the DFT spectra (~171 → **163** cm^{-1}), indicating overlapping contributions from different modes. A complementary DFT simulation for the $[4Fe–4S]_H{}^{2+}$ $–Fe_p(II)Fe_d(I)$ redox state of the H-cluster, H_{ox}, reveals comparable ^{12}CH → **^{13}CD** spectral shifts in the broader ~150–330 cm^{-1} region (Figure S2); this indicates that the ADT labeling effects observed in NRVS are stable against potential impurities from additional redox states of the H-cluster.

The atomic motions deduced from the DFT calculations on H_{hyd} are displayed in Figure 3 and animated as part of the Supporting Information. The **162** cm^{-1} band of **^{13}CD-1**-*Cr*HydA1 contains $[2Fe]_H$ modes heavily mixed with the protein environment, but an important feature here is rocking of the $–NH_{ADT}–$ bridgehead toward the distal iron hydride

Fe_d–H_h, along with out-of-phase rotation of the ADT –$^{13}CD_2$– groups; this character matches the **^{13}CD-1** precursor mode at **143** cm^{-1}. At higher energies, the **291** cm^{-1} mode exhibits a breathing motion of the Fe_2S_2 moiety, which leads to changing the distance between Fe_p and the $[4Fe–4S]_H$ cluster; in this case, there is an in-phase motion of the ADT methylene groups in the opposite direction of the amine bridgehead, similar to the **^{13}CD-1** mode at **314** cm^{-1} described above. The **308** cm^{-1} mode exhibits an entire ADT fragment wagging/rotation relative to Fe_p and Fe_d, equivalent to the **^{13}CD-1** mode at **287** cm^{-1}. We also illustrate the **73** cm^{-1} mode, which is highly delocalized with torsional motions of the entire H-cluster.

We now turn to the higher-energy side of the H_{hyd} spectra, which contains two distinct Fe_d–H_h bending mode peaks observed at 679/**676** and 748/**746** cm^{-1}, and calculated at 670/**670** and 753/**750** cm^{-1} (Figure 3). These were the focus of previous studies because they characterize the terminal iron hydride bonding and its interactions with the surroundings.[20–22] The two main features arise from the relatively pure H_h hydride bending motion perpendicular to and parallel to the plane defined by the Fe_p–Fe_d axis and the Fe_d–H_h bond, respectively. Although the isotope-dependent shifts in these bands are small and nearly unmeasurable, the fine structure of the underlying normal modes displays a difference. In the current DFT analysis there are **1**-/**^{13}CD-1**-*Ct*HydA1 “perpendicular” modes at 670/**665**,**671** cm^{-1}, and “parallel” modes at 752,754/**749**,**758** cm^{-1} respectively. The ^{13}CD-labeling introduces N_{ADT}–H_{ADT} bending admixtures to the Fe_d–H_h modes, where the H_{ADT} and H_h nuclei displace either in- or out-of-phase; e.g., the **758** cm^{-1} “parallel” mode (Figure 3) brings H_h and H_{ADT} closer during half of each excursion cycle. The calculations suggest an increased involvement of the heavier ^{13}CD-ADT fragment in the Fe_d–H_h bends, with rotations of the two –$^{13}CD_2$– methylene groups contributing at least 16% to the vibrational kinetic energy. Similar modes are calculated in the ADT-labeled **^{13}CD-1** precursor in the ~670–770 cm^{-1} region, while the unlabeled (^{12}CH–)**1** variant produces their counterparts at frequencies only above 800 cm^{-1} (Table S2).

The DFT analysis therefore indicates that some modes in the Fe_d–H_h bending region involve mixing with motions inherent to the ^{13}CD-labeled ADT ligand. A search for such “satellite” modes is what initially prompted our isotopic labeling investigation. The experimental data might show weak “satellite” features on either side of the main Fe_d–H_h bending peaks (Figure 3). However, despite prolonged data collection in this region to improve the signal-to-noise (S/N) ratio, firm assignment of the small differences to “satellites” is not yet possible. The exact calculated energies of the “satellites” should also be taken with caution, because they are governed by motion of a very light H_h nucleus that mediates interaction between $^{57}Fe_d$ and the ADT bridgehead. Further experimental insight into these modes will require a significantly higher NRVS photon flux, which may be available in the next generation of synchrotron sources, e.g., PETRA-IV.[37]

The accuracy of the DFT calculations at reproducing the experimental NRVS spectra of the unlabeled and isotopically labeled precursor and $[2Fe]_H$, here and in our previous work,[20–22,36] gives us confidence that it is valuable to consider the predicted “satellite” modes in H_{hyd}, whether or not they can be conclusively detected by NRVS. Illustrations of these “satellite” modes at **720** and **765** cm^{-1} are included in Figure 3. The latter two modes

involve "parallel" Fe_d–H_h bending, similar to the **749** and **758** cm^{-1} modes. Interestingly, some of these modes involve motion of the nearby cysteine at the end of the proton transfer channel leading to the ADT ligand. These vibrational modes appear to represent a pathway for coupled proton transfer from (C169)S_C–H_C to N_{ADT} and from N_{ADT}–H_{ADT} to Fe_d–H_h.

Are any other modes relevant to H_2 production catalysis? We inspected the DFT calculations for changes in $H_{ADT}\cdots H_h$ and $N_{ADT}\cdots H_C$ distances that occur during normal mode displacements (see Figure S3). The results for the modes with the greatest distance changes are summarized in Table S1. The equilibrium 2.06 Å $H_{ADT}\cdots H_h$ distance is already firmly in the 1.7–2.2 Å range for a "dihydrogen bond",[38] and it is similar to the 2.02 Å value seen as the shortest H···H distance in solid BH_3NH_3.[39] We found that a few modes contribute a disproportionate amount of motion involving the $H_{ADT}\cdots H_h$ distance as well as the $N_{ADT}\cdots H_C$ distance. In particular, the "parallel" Fe_d–H_h bending modes at 752/**758** cm^{-1} yield the record ~0.14/**0.15** Å contractions in the $H_{ADT}\cdots H_h$ distance across the entire vibrational spectra. For the $N_{ADT}\cdots H_C$ distance, the largest vibrational contraction of ~0.11 Å is achieved in the S_C–H_C stretching mode calculated at 2449/**2449** cm^{-1}.

From time-resolved photochemical IR studies, Sanchez et al. have shown that the decay of H_{hyd} is kinetically competent as a near-final step in the [FeFe] hydrogenase catalytic cycle.[40] However, since the pK_a for a neutral secondary amine such as the ADT bridgehead nitrogen is extremely high, an intervening protonated ADT $-NH_2^+-$ intermediate, $H_{hyd}H^+$, has often been included in the catalytic cycle.[17,24,41–44] Our results, which document the role of ADT flexibility in normal modes that bring H_{ADT} and H_h closer together, offer the possibility of a mechanism update.

In this speculative scenario, high-frequency modes such as at 752/**758** and 2449/**2449** cm^{-1}, combined with low-frequency modes such as at **73** cm^{-1}, would involve coordinated motion of H_{ADT} toward H_h, while H_C moves toward N_{ADT}. This might precipitate a "deep tunneling" transfer of H_{ADT} to H_h, while S_C–H_C transfer replenishes the N_{ADT}–H_{ADT}, and with the S_C–H_C proton reloaded from the H_2O in the proton transfer chain. Champion and co-workers have shown that deep tunneling can allow high pK_a residues to participate in proton transfer chains, as invoked for a serine residue in the green fluorescent protein.[45] If the transfer reaction for H_{hyd} were facilitated by electron transfer from the $[4Fe–4S]_H^+$ to the $[Fe^{II}Fe^{II}]_H$ subsite, the overall PCET reaction would yield an H_{ox} electronic state with bound H_2. This scenario agrees with calculations on the reverse reaction of H_2 activation by Greco et al.[46]

In summary, we have investigated vibrations of the [FeFe] hydrogenase active site in the H_{hyd} state through ^{57}Fe, ^{13}C, and D isotopic labeling, combined with ^{57}Fe NRVS measurements and DFT calculations. This represents the first observation of second and third coordination sphere isotope effects using NRVS. We identified normal modes involving the flexing of the bridging ADT ligand that point to its unique properties as an active site ligand. The combined motions of the Fe_d–H_h, N_{ADT}–H_{ADT}, and (C169)S_C–H_C protons are presumably coupled to the remainder of the proton transfer chain as well as electron transfer. These effects may be important for catalysis and will be investigated in future studies.

Supplementary Material

Refer to Web version on PubMed Central for supplementary material.

ACKNOWLEDGMENTS

V.P. acknowledges funding by the Deutsche Forschungsge-meinschaft (DFG, German Research Foundation) under Germany's Excellence Strategy, EXC 2008-390540038, UniSysCat. J.A.B. acknowledges funding from the DFG SPP 1927 "Iron-Sulfur for Life" project (Project BI 2198/1-1). E.J.R., J.A.B., and W.L. would like to thank the Max Planck Society for continuous financial support. The contributions of T.B.R. and C.P.R. were funded by the U.S. National Institutes of Health through GM61153. S.P.C. was funded by NIH GM65440. Some computational work was performed under the XSIM project on the CORI computing system at NERSC, a U.S. Department of Energy Office of Science User Facility operated under Contract DE-AC02-05CH11231. The authors gratefully acknowledge the assistance by Giorgio Caserta in acquisition of the NRVS data.

REFERENCES

(1). Glenk G; Reichelstein S Economics of converting renewable power to hydrogen. Nat. Energy 2019, 4 (3), 216–222.

(2). Armaroli N; Balzani V The Hydrogen Issue. ChemSusChem 2011, 4 (1), 21–36. [PubMed: 21226208]

(3). Ávila Neto C; Dantas SC; Silva FA; Franco TV; Romanielo L; Hori C; Assis AJ Hydrogen production from methane reforming: Thermodynamic assessment and autothermal reactor design. J. Nat. Gas Sci. Eng 2009, 1, 205–215.

(4). Hosseini SE; Wahid MA Hydrogen from solar energy, a clean energy carrier from a sustainable source of energy. Int. J. Energy Res 2020, 44 (6), 4110–4131.

(5). Ren XF; Lv QY; Liu LF; Liu BH; Wang YR; Liu AM; Wu G Current progress of Pt and Pt-based electrocatalysts used for fuel cells. Sust. En. Fuels 2020, 4 (1), 15–30.

(6). Bullock RM; Helm ML Molecular Electrocatalysts for Oxidation of Hydrogen Using Earth-Abundant Metals: Shoving Protons Around with Proton Relays. Acc. Chem. Res 2015, 48 (7), 2017–2026. [PubMed: 26079983]

(7). Fukuzumi S; Lee YM; Nam W Thermal and photocatalytic production of hydrogen with earth-abundant metal complexes. Coord. Chem. Rev 2018, 355, 54–73.

(8). Lubitz W; Ogata H; Rüdiger O; Reijerse E Hydrogenases. Chem. Rev 2014, 114 (8), 4081–4148. [PubMed: 24655035]

(9). Peters JW; Schut GJ; Boyd ES; Mulder DW; Shepard EM; Broderick JB; King PW; Adams MWW [FeFe]-and [NiFe]-hydrogenase diversity, mechanism, and maturation. Biochim. Biophys. Acta, Mol. Cell Res 2015, 1853 (6), 1350–1369.

(10). Esselborn J; Muraki N; Klein K; Engelbrecht V; Metzler-Nolte N; Apfel UP; Hofmann E; Kurisu G; Happe T A structural view of synthetic cofactor integration into [FeFe]-hydrogenases. Chem. Sci 2016, 7 (2), 959–968. [PubMed: 29896366]

(11). Wittkamp F; Senger M; Stripp ST; Apfel UP FeFe-Hydrogenases: recent developments and future perspectives. Chem. Commun 2018, 54 (47), 5934–5942.

(12). Cornish AJ; Gartner K; Yang H; Peters JW; Hegg EL Mechanism of Proton Transfer in FeFe-Hydrogenase from *Clostridium pasteurianum*. J. Biol. Chem 2011, 286 (44), 38341–38347. [PubMed: 21900241]

(13). Hong G; Cornish AJ; Hegg EL; Pachter R On understanding proton transfer to the biocatalytic $[Fe\text{-}Fe]_H$ sub-cluster in [Fe-Fe] H_2 ases: QM/MM MD simulations. Biochim. Biophys. Acta, Bioenerg 2011, 1807 (5), 510–517.

(14). Knörzer P; Silakov A; Foster CE; Armstrong FA; Lubitz W; Happe T Importance of the Protein Framework for Catalytic Activity of FeFe-Hydrogenases. J. Biol. Chem 2012, 287 (2), 1489–1499. [PubMed: 22110126]

(15). Long H; King PW; Chang CH Proton Transport in *Clostridium pasteurianum* FeFe Hydrogenase I: A Computational Study. J. Phys. Chem. B 2014, 118 (4), 890–900. [PubMed: 24405487]

(16). Ginovska-Pangovska B; Ho MH; Linehan JC; Cheng YH; Dupuis M; Raugei S; Shaw WJ Molecular dynamics study of the proposed proton transport pathways in FeFe-hydrogenase. Biochim. Biophys. Acta, Bioenerg 2014, 1837 (1), 131–138.

(17). Mulder DW; Ratzloff MW; Bruschi M; Greco C; Koonce E; Peters JW; King PW Investigations on the Role of Proton-Coupled Electron Transfer in Hydrogen Activation by FeFe-Hydrogenase. J. Am. Chem. Soc 2014, 136 (43), 15394–15402. [PubMed: 25286239]

(18). Mulder DW; Guo Y; Ratzloff MW; King PW Identification of a Catalytic Iron-Hydride at the H-Cluster of [FeFe]-Hydrogenase. J. Am. Chem. Soc 2017, 139, 83–86. [PubMed: 27973768]

(19). Silakov A; Wenk B; Reijerse E; Lubitz W ^{14}N HYSCORE investigation of the H-cluster of FeFe hydrogenase: evidence for a nitrogen in the dithiol bridge. Phys. Chem. Chem. Phys 2009, 11 (31), 6592–6599. [PubMed: 19639134]

(20). Reijerse EJ; Pham CC; Pelmenschikov V; Gilbert-Wilson R; Adamska-Venkatesh A; Siebel JF; Gee LB; Yoda Y; Tamasaku K; Lubitz W; Rauchfuss TB; Cramer SP Direct observation of an iron bound terminal hydride intermediate in [FeFe] hydrogenase. J. Am. Chem. Soc 2017, 139 (12), 4306–4309. [PubMed: 28291336]

(21). Pelmenschikov V; Birrell JA; Pham CC; Mishra N; Wang HX; Sommer C; Reijerse E; Richers CP; Tamasaku K; Yoda Y; Rauchfuss TB; Lubitz W; Cramer SP Reaction Coordinate Leading to H_2 Production in [FeFe] Hydrogenase Identified by Nuclear Resonance Vibrational Spectroscopy and Density Functional Theory. J. Am. Chem. Soc 2017, 139 (46), 16894–16902. [PubMed: 29054130]

(22). Pham CC; Mulder DW; Pelmenschikov V; King PW; Ratzloff MW; Wang H; Mishra N; Alp EE; Zhao J; Hu MY; Tamasaku K; Yoda Y; Cramer SP Terminal Hydride Species in [FeFe]-Hydrogenases are Vibrationally Coupled to the Active Site Environment. Angew. Chem., Int. Ed 2018, 57, 10605–10609.

(23). Rumpel S; Sommer C; Reijerse E; Fares C; Lubitz W Direct Detection of the Terminal Hydride Intermediate in FeFe Hydrogenase by NMR Spectroscopy. J. Am. Chem. Soc 2018, 140 (11), 3863–3866. [PubMed: 29521088]

(24). Lorent C; Katz S; Duan J; Kulka CJ; Caserta G; Teutloff C; Yadav S; Apfel U-P; Winkler M; Happe T; Horch M; Zebger I Shedding light on proton and electron dynamics in [FeFe] hydrogenases. J. Am. Chem. Soc 2020, 142, 5493–5497. [PubMed: 32125830]

(25). Seto M; Yoda Y; Kikuta S; Zhang XW; Ando M Observation of Nuclear Resonant Scattering Accompanied by Phonon Excitation Using Synchrotron Radiation. Phys. Rev. Lett 1995, 74, 3828–3831. [PubMed: 10058307]

(26). Chumakov A; Rüffer R Nuclear inelastic scattering. Hyperfine Interact. 1998, 113 (1), 59–79.

(27). Scheidt WR; Li JF; Sage JT What Can Be Learned from Nuclear Resonance Vibrational Spectroscopy: Vibrational Dynamics and Hemes. Chem. Rev 2017, 117 (19), 12532–12563. [PubMed: 28921972]

(28). Hu MY Some notes on data analysis for nuclear resonant inelastic x-ray scattering. Hyperfine Interact. 2016, 237, 64.

(29). Sage JT; Paxson C; Wyllie GRA; Sturhahn W; Durbin SM; Champion PM; Alp EE; Scheidt WR Nuclear resonance vibrational spectroscopy of a protein active-site mimic. J. Phys.: Condens. Matter 2001, 13, 7707–7722.

(30). Leu BM; Zgierski MZ; Wyllie GRA; Scheidt WR; Sturhahn W; Alp EE; Durbin SM; Sage JT Quantitative Vibrational Dynamics of Iron in Nitrosyl Porphyrins. J. Am. Chem. Soc 2004, 126 (13), 4211–4227. [PubMed: 15053610]

(31). Cramer SP Nuclear Resonance Vibrational Spectroscopy. In X-Ray Spectroscopy with Synchrotron Radiation: Fundamentals and Applications; Springer International Publishing: Cham, 2020; pp 257–278.

(32). Reijerse EJ; Pelmenschikov V; Birrell JA; Richers CP; Kaupp M; Rauchfuss TB; Cramer SP; Lubitz W Asymmetry in the Ligand Coordination Sphere of the [FeFe] Hydrogenase Active Site Is Reflected in the Magnetic Spin Interactions of the Azapropanedithiolate Ligand. J. Phys. Chem. Lett 2019, 10 (21), 6794–6799. [PubMed: 31580680]

(33). Berggren G; Adamska A; Lambertz C; Simmons TR; Esselborn J; Atta M; Gambarelli S; Mouesca JM; Reijerse E; Lubitz W; Happe T; Artero V; Fontecave M Biomimetic assembly and activation of FeFe-hydrogenases. Nature 2013, 499 (7456), 66. [PubMed: 23803769]

(34). Han S; Czernuszewicz RS; Kimura T; Adams MWW; Spiro TG Fe_2S_2 Protein Resonance Raman Revisited: Structural Variations among Adrenodoxin, Ferredoxin, and Red Paramagnetic Protein. J. Am. Chem. Soc 1989, 111 (10), 3505–3511.

(35). Fu W; Drozdzewski PM; Davies MD; Sligar SG; Johnson MK Resonance Raman and Magnetic Circular Dichroism Studies of Reduced [2Fe-2S] Proteins. J. Biol. Chem 1992, 267 (22), 15502–15510. [PubMed: 1639790]

(36). Birrell JA; Pelmenschikov V; Mishra N; Wang H; Yoda Y; Tamasaku K; Rauchfuss TB; Cramer SP; Lubitz W; DeBeer S Spectroscopic and Computational Evidence that [FeFe] Hydrogenases Operate Exclusively with CO-Bridged Intermediates. J. Am. Chem. Soc 2020, 142 (1), 222–232. [PubMed: 31820961]

(37). Schroer CG; Agapov I; Brefeld W; Brinkmann R; Chae YC; Chao HC; Eriksson M; Keil J; Nuel Gavalda X; Rohlsberger R; Seeck OH; Sprung M; Tischer M; Wanzenberg R; Weckert E PETRA IV: the ultralow-emittance source project at DESY. J. Synchrotron Radiat 2018, 25 (5), 1277–1290. [PubMed: 30179167]

(38). Custelcean R; Jackson JE Dihydrogen Bonding: Structures, Energetics, and Dynamics. Chem. Rev 2001, 101 (7), 1963–1980. [PubMed: 11710237]

(39). Klooster WT; Koetzle TF; Siegbahn PEM; Richardson TB; Crabtree RH Study of the N—H. H—B dihydrogen bond including the crystal structure of BH_3NH_3 by neutron diffraction. J. Am. Chem. Soc 1999, 121 (27), 6337–6343.

(40). Sanchez MLK; Sommer C; Reijerse E; Birrell JA; Lubitz W; Dyer RB Investigating the Kinetic Competency of CrHydA1 FeFe Hydrogenase Intermediate States via Time-Resolved Infrared Spectroscopy. J. Am. Chem. Soc 2019, 141 (40), 16064–16070. [PubMed: 31509403]

(41). Sommer C; Adamska-Venkatesh A; Pawlak K; Birrell JA; Rudiger O; Reijerse EJ; Lubitz W Proton Coupled Electronic Rearrangement within the H-Cluster as an Essential Step in the Catalytic Cycle of FeFe Hydrogenases. J. Am. Chem. Soc 2017, 139 (4), 1440–1443. [PubMed: 28075576]

(42). Duan JF; Senger M; Esselborn J; Engelbrecht V; Wittkamp F; Apfel UP; Hofmann E; Stripp ST; Happe T; Winkler M Crystallographic and spectroscopic assignment of the proton transfer pathway in FeFe-hydrogenases. Nat. Commun 2018, 9, 4726. [PubMed: 30413719]

(43). Ratzloff MW; Artz JH; Mulder DW; Collins RT; Furtak TE; King PW CO-Bridged H-Cluster Intermediates in the Catalytic Mechanism of FeFe-Hydrogenase CaI. J. Am. Chem. Soc 2018, 140 (24), 7623–7628. [PubMed: 29792026]

(44). Arrigoni F; Bertini L; Bruschi M; Greco C; De Gioia L; Zampella G H_2 Activation in [FeFe]-Hydrogenase Cofactor Versus Diiron Dithiolate Models: Factors Underlying the Catalytic Success of Nature and Implications for an Improved Biomimicry. Chem. - Eur. J 2019, 25 (5), 1227–1241. [PubMed: 30475417]

(45). Salna B; Benabbas A; Sage JT; van Thor J; Champion PM Wide-dynamic-range kinetic investigations of deep proton tunnelling in proteins. Nat. Chem 2016, 8 (9), 874–880. [PubMed: 27554414]

(46). Greco C; Bruschi M; Fantucci P; Ryde U; De Gioia L Mechanistic and physiological implications of the interplay among iron-sulfur clusters in [FeFe]-hydrogenases. A QM/MM perspective. J. Am. Chem. Soc 2011, 133 (46), 18742–9. [PubMed: 21942468]

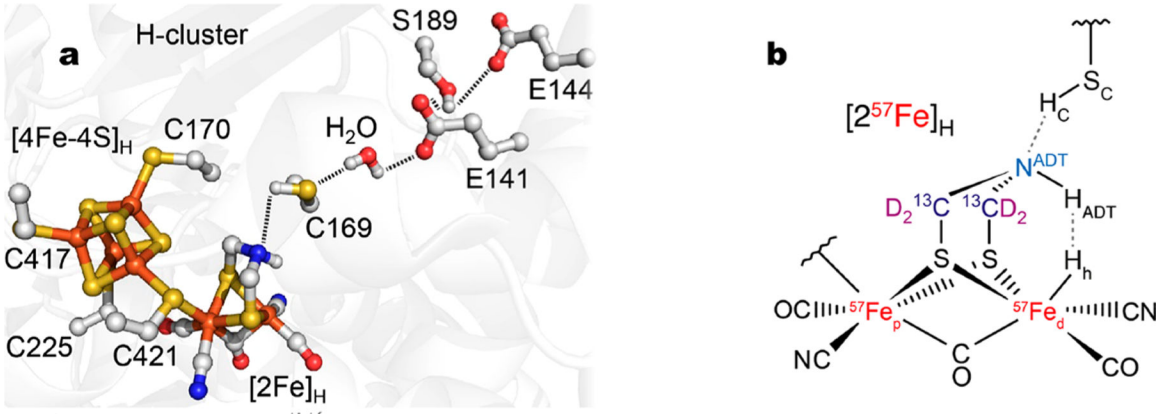

Figure 1.

(a) [FeFe] hydrogenase active site including key amino acids in the proton transfer pathway (based on the PDB 4XDC[10] structure of the *Cp*I enzyme from *Clostridium pasteurianum*, but using *Cr*HydA1 sequence numbering). (b) Schematic structure of the $[2Fe]_H$ subcluster in the H_{hyd} state, showing the isotopically labeled nuclei ^{57}Fe, ^{13}C, and D (i.e. ^{2}H). The important hydrogens, H_h (catalytic hydride at the distal Fe_d iron), H_{ADT} (at the ADT N_{ADT} nitrogen), and H_C (at the S_C C169 sulfur), are shown.

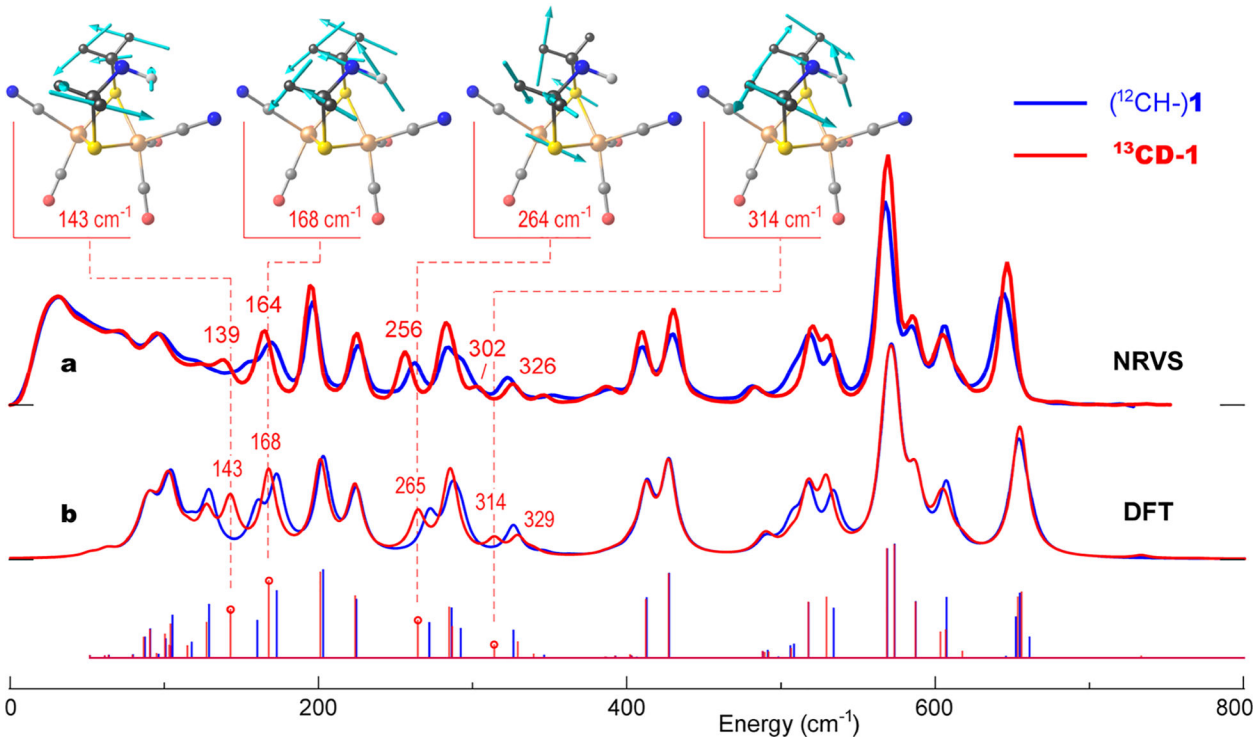

Figure 2.

^{57}Fe-PVDOS for the $[2Fe]_H$ precursor isotopologues **1** (blue) vs **^{13}CD-1** (red) from (a) NRVS experiments and (b) DFT calculations. Sticks correspond to individual DFT normal mode energies and intensities before lineshape convolution. For **^{13}CD-1**, important band positions are labeled, and atomic motions in selected normal modes are shown.

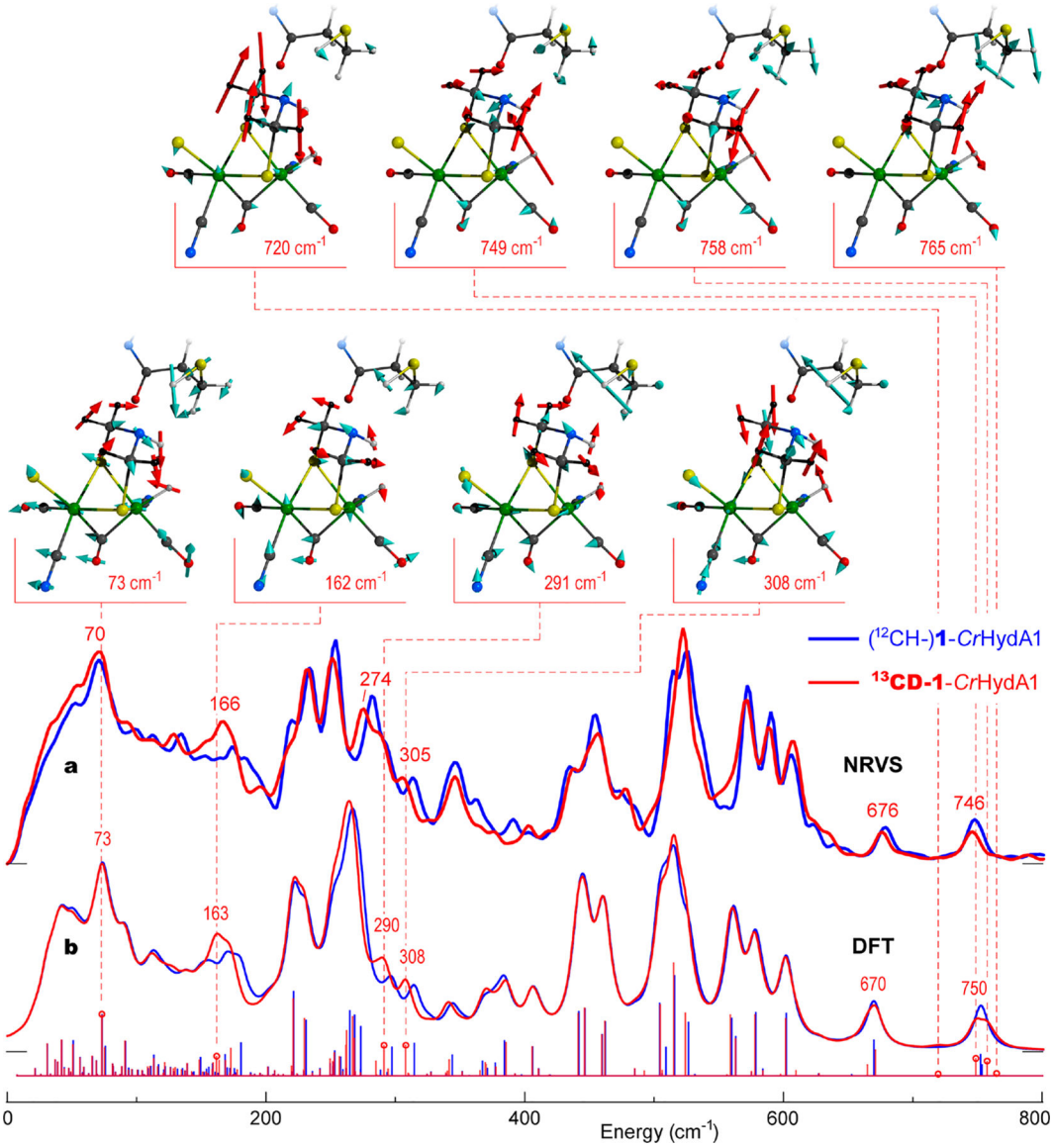

Figure 3.

^{57}Fe-PVDOS for the H_{hyd} state isotopologues **1-***Cr*HydA1 (blue) vs **^{13}CD-1-***Cr*HydA1 (red) from (a) an NRVS experiment and (b) DFT calculations. Sticks correspond to individual DFT normal mode energies and intensities before broadening. For **^{13}CD-1-***Cr*HydA1, important band positions are labeled, and atomic motions in selected normal modes are shown. Only the $[2Fe]_H$ and C169 fragments of the DFT model are shown with the methylene, H_h, and H_{ADT} hydrogen nuclei displacements indicated by red arrows.